

Observations and 3D Hydrodynamical models of planetary nebulae with Wolf Rayet type central stars ^{*}

Rechy-García, J. S. ¹†, Velázquez, P. F. ², Peña. M.¹, Raga, A. C.²

¹*Instituto de Astronomía, Universidad Nacional Autónoma de México, Apdo. Postal 70264, 04510, Ciudad de México, México.*

²*Instituto de Ciencias Nucleares, Universidad Nacional Autónoma de México, Apdo. Postal 70543, 04510, Ciudad de México, México.*

ABSTRACT

We present high-resolution, long-slit spectroscopic observations of two planetary nebulae with [WC] central stars located near the galactic bulge, M 1-32 and M 3-15. The observations were obtained with the 2.1-m telescope at the Observatorio Astronómico Nacional, San Pedro Mártir. M 1-32 shows wide wings on the base of its emission lines and M 3-15 has two very faint high-velocity knots. In order to model both PNe we built a three-dimensional model consisting of a jet interacting with an equatorially concentrated slow wind, emulating the presence of a dense torus, using the Yguazú hydrodynamical code. From our hydrodynamical models, we obtained position-velocity (PV) diagrams in the [N II] λ 6583 line for comparison with the observations. We find that the spectral characteristics of M 1-32 and M 3-15 can be explained with the same physical model -a jet moving inside an AGB wind- using different parameters (physical conditions and position angles of the jet). In agreement with our model and observations, these objects contain a dense torus seeing pole-on and a bipolar jet escaping thorough the poles. Then we propose to classify this kind of objects as spectroscopic bipolar nebulae, although they have been classified morphologically as compact, round, or elliptical nebulae or with "close collimated lobes".

Key words: Planetary nebulae: general — hydrodynamics — methods: observational — methods: numerical — ISM: jets and outflows.

1 INTRODUCTION

Planetary nebulae (PNe) represent a highly evolved stage of low-intermediate mass stars (1-8 M_{\odot}). Several thousand objects are known in the Milky Way and chemical abundances have been determined in a large number of them which has led to classify them as Type I (N and He-rich young objects), Type II (objects in the galactic disk with peculiar velocities lower than 60 km s⁻¹), Type III (objects with peculiar velocities larger than 60 km s⁻¹), and Type IV (old objects belonging to the extreme Population II, see Peimbert 1990). Thus, PNe of different types belong to different populations in the galaxy.

In addition, PNe are classified by their morphology: they can be round, compact, elliptical, bipolar, or point-symmetric nebulae (see for example, Balick 1987; Manchado et al. 1996). More recently, Sahai et al. (2011) proposed a more detailed morphological classification for young PNe,

based on deep, high-resolution imaging from HST. We will refer to this classification later on. However, in many cases it is difficult to decide which is the real morphology of a PN, because we need to consider different aspects. For example the projection effects of a three dimensional object on the plane of the sky, the exposure time dependence on the object morphology, or observations in lines of different ions give different morphologies due to the stratification in the nebula. Despite these complications, the study of morphology plays an important role for understanding the ejection processes, the presence of magnetic fields and even the presence of a binary central star.

Approximately 80% of PNe are asymmetric (Parker et al. 2006; Douchin et al. 2013), showing ellipsoidal, bipolar or multipolar morphologies, displaying tori, jets, knots, etc. How can the formation of such components be explained? Pascoli (1992) proposed that the magnetic field can produce a bipolar morphology in PNe. Also García-Segura et al. (1999) suggested that asymmetries can be due to magnetic fields and stellar rotation. Soker & Harpaz (1992) had already shown that even if the magnetic field works for shaping asymmetric PNe, a binary companion is necessary. The notion that magnetic fields alone are insufficient for shap-

^{*} Based upon observations carried out at the Observatorio Astronómico Nacional on the Sierra San Pedro Mártir (OAN-SPM), Baja California, México.

† E-mail: jrechy@astro.unam.mx

ing bipolar morphologies has been subsequently reinforced by Soker (2006), Nordhaus et al. (2007), and García-Segura et al. (2014).

The conception of a binary system as the shaping mechanism of bipolar and multipolar PNe has several decades (Bond et al. 1978; Livio et al. 1979; Soker & Livio 1994; De Marco 2009). Bond (2000) showed that there is a considerable circumstantial evidence about the role played by close-binary systems (or post-common envelope systems, post CE) in the formation and shaping elliptical or bipolar planetary nebulae. Tocknell et al. (2014) found that post CE central stars often have jets. De Marco et al. (2008) showed that at least 10%–15% of PNe have binary systems with short orbital periods (<3 days), giving strong support to the binary hypothesis as shaping mechanism. Several more binary systems in PNe have been reported by Miszalski et al. (2009).

Bipolar PNe can be formed by two jets which are ejected by one of the components of a binary system (Morris 1987; Soker & Rappaport 2000). Sahai & Trauger (1998) (see also Balick & Frank 2002) showed that these jets play a primary role in forming bipolar proto PNe (PPNe). García-Arredondo & Frank (2004) carried out a 3D hydrodynamical simulation of the interaction between an AGB wind and a jet, showing that bipolar morphologies are obtained for the strong jet case (when the jet momentum is larger than the AGB wind momentum). Dennis et al. (2008) showed that “jetlike” outflows in PPN can be formed by the launching of clumps or bullets from one of the components of the binary system. Employing the hypothesis of a binary system in the centre of the nebula, Riera et al. (2014) and Velázquez et al. (2014) modelled the morphology and proper motions of the PPNe CRL 618 by means of a precessing jet with a time-dependent ejection velocity, obtaining a good agreement with observations. We will use these ideas in this work.

A special group of PNe (around 10%) has a central star which displays strong and very wide emission lines, evidence that they are suffering atmospheric instabilities with large mass loss. These stars show spectra similar to the massive Wolf-Rayet stars of the C sequence and they have been classified as [WC]. Their atmospheres are deficient in H, showing mainly He, C and O (Koesterke 2001). PNe with central stars of the [WC] type (hereafter [WC]PN) have larger expansion velocities and present more turbulence than PNe with normal central stars (Medina et al. 2006). (Peña et al. 2013) found that the [WC]PNe are more concentrated towards the galactic thin disk (height smaller than about 400 pc from the disk), compared to PNe with normal central stars, most of which are distributed up to 800 pc from the disk. This has been interpreted as evidence that [WC]PNe belong to a younger population than PNe with normal stars.

In this work we aim to analyze the kinematical behavior of two [WC]PNe, named M1-32 and M3-15, which show evidence of having jets at high velocities and to relate their kinematics with other nebular characteristics.

M1-32 (PN G 011.9+04.2) has a [WO4]pec central star (Acker & Neiner 2003; Weidmann & Gamen 2011) and presents some very interesting characteristics, some of which are listed in Table 1. It is located towards the galactic bulge, showing a high heliocentric radial velocity of -86.4 km s^{-1} (Peña et al. 2013). Its heliocentric distance is 4.79 kpc (Stanghellini & Haywood 2010). It is a moderate Peimbert Type I PN (with a N/O abundance ratio of 0.50

and a He/H ratio of 0.126) and shows a large C-enrichment, with a C/O abundance ratio of 4.3 (García-Rojas et al. 2013). Evolution models for single stars by Karakas (2010) indicate that such a nebular C-enrichment should have been produced by a central star with an initial mass larger than $3 M_{\odot}$. This high initial stellar mass can also explain the high N/O abundance in the nebula. Morphologically it has been classified as an elliptical nebula (Stanghellini & Haywood 2010) but, from high-resolution spectra Medina et al. (2006) found that the nebular lines present intense narrow profiles with faint wide wings. In addition, from spectroscopic analysis it is found that the nebular morphology of M1-32 is highly asymmetric, showing a dense, almost face-on torus with low expansion velocity, and also knots and jets at high velocities of $\pm 200 \text{ km s}^{-1}$. There is also evidence of a possible external envelope (Akras & López 2012).

PN G 006.8+04.1, also known as M3-15, has a [WC4] central star (Acker & Neiner 2003; Weidmann & Gamen 2011) and it has been classified as compact (López et al. 2012). It is located towards the galactic bulge, showing a high heliocentric radial velocity of 96.9 km s^{-1} (Peña et al. 2013). Its heliocentric distance is 6.82 kpc (Stanghellini & Haywood 2010). In Table 1 we list some of its characteristics. Medina et al. (2006) found that the line profiles show a narrow component, with an expansion velocity of 20 km s^{-1} and two faint knots at velocities of $\pm 90 \text{ km s}^{-1}$ (see also Akras & López 2012). The total nebular abundance ratios in this object are $C/O = 0.467$, $N/O = 0.14$ y $He/H = 0.107$ (García-Rojas et al. 2013); therefore, differently from M1-32, this object is not a Type I PN and it does not show C-enrichment.

In the recent morphological classification scheme proposed by Sahai et al. (2011), based on HST imaging, they classify M3-15 as a “L,c bcr(c) ps(s)” nebula, meaning that it has close collimated lobes, with a close “barrel-shaped” central region, and the overall geometric shape of the lobes is point-symmetric (see Figure 6 of Sahai et al. 2011). There are no high-resolution images available for M1-32, so that Sahai et al. (2011) classification cannot be directly applied, but in Figure 1 we present an image in $H\alpha$ of M1-32 obtained by us which clearly shows that the shape for this PN is a “face-on torus”.

In this work, we use high resolution spectra to analyze the kinematical behavior of the gas in these two [WC]PNe, and by using a hydrodynamical model we investigate if the morphological structure of M1-32 and M3-15 can be produced by the interaction between a jet and a dense torus. We compare the position-velocity diagrams obtained from the observations with those predicted by the hydrodynamical models.

The paper is organized as follows. In §2, the spectral observations are presented. In §3, we describe the hydrodynamical model which has been calculated with the code Yguazú (Raga et al. 2000). In §4 we discuss the results for each object and in §5 we summarize the main conclusions.

2 OBSERVATIONS

High-resolution spectra for both planetary nebulae were obtained with the Manchester Echelle Spectrometer (MES,

Table 1. Main characteristics of M 1-32 and M 3-15

PN G	Name	Spectral Type	V_{hel} km s ⁻¹	D kpc	C/H ^a	N/H ^a	O/H ^a
006.8+04.1	M 3-15	[WC 4]	96.9±0.8	6.82±1.365	8.85±0.13	8.33±0.10	9.18±0.08
011.9+04.2	M 1-32	[WO 4] pec	-86.4±0.8	4.79±0.959	9.75±0.09	8.44±0.06	9.11±0.08

^a In $12 + \log X/H$ (see García-Rojas et al. (2013))

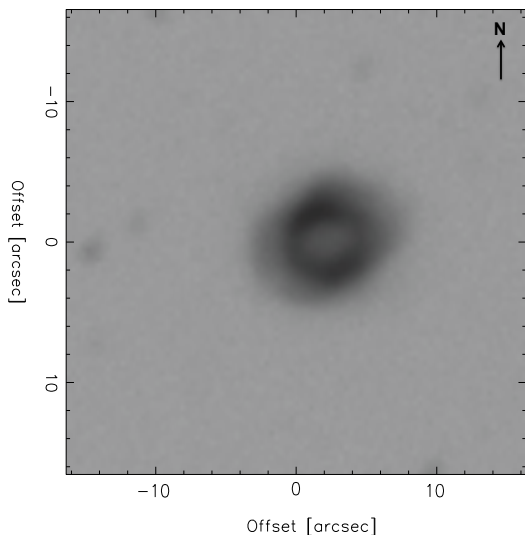


Figure 1. $H\alpha$ image of PN M 1-32, obtained that OAN-SPM using MES spectrograph. North is up and East to the left. The exposure time is 100 s. We observe a face-on torus and a possible external envelope.

Meaburn et al. 2003) attached to the 2.1-m telescope of the Observatorio Astronómico Nacional at San Pedro Mártir, B.C, Mexico (OAN-SPM). The MES is a long-slit echelle spectrometer, which uses narrow-band filters to isolate the orders containing the emission lines of interest. In our case, the filters used isolated the order corresponding to $H\alpha$ (this order includes the $H\alpha$, $[N II]\lambda 6548$ and $[N II]\lambda 6583$ emission lines) and the order isolating the $[O III]\lambda 5007$ emission line. In this paper, we only show the behavior of the $[N II]\lambda 6548$ line because the other lines show the same structure.

The MES was equipped with a Marconi 2 CCD detector, which has a pixel size of $13.5 \mu m$. A binning of 2×2 was applied and, using the secondary mirror $f/7.5$ which provides a plate scale of $13.2''/mm$, the plate scale on the detector was $0.356''/pixel$. The slit width used was $150 \mu m$ (equivalent to $2''$ on the sky) and it was oriented north-south. The spectral resolution obtained is of 11 km s^{-1} .

Observations were obtained for three different regions of the object (see Figs. 2 and 3). Immediately after every science observation, exposures of a Th-Ar lamp were acquired for wavelength calibration. The internal precision of the lamp calibrations is better than 1.0 km s^{-1} . Data re-

Table 2. Log of observations

PN G	Name	Date	slit pos., PA	Exp. time (s)
006.8+04.1	M 3-15	05/08/2011	East, 0°	600
			Centre, 0°	1200
			West, 0°	1200
011.9+04.2	M 1-32	04/08/2011	East, 0°	1200
			Centre, 0°	1200
			West, 0°	600

duction was performed using the standard processes for the MES, with IRAF¹ reduction packages. In Table 2 we present the log of the observations.

2.1 PV diagrams

PV diagrams for each PN were obtained with the WIP software (Morgan 1995). In Fig. 2 the PV diagrams for M 1-32 are shown for the slit located in three different positions (East, Centre, and West, as it is shown in the left side of this figure). In the horizontal axis the heliocentric radial velocity is represented and the vertical axis shows the spatial direction. The emission line shown in these spectra is $[N II]\lambda 6548$. In the central position diagram two bright knots (at a heliocentric systemic velocity of -86.4 km s^{-1}) and wings at high velocities are visible. These wings have velocities of $\pm 180 \text{ km s}^{-1}$, relative to the systemic velocity.

Fig. 3 shows the PV diagrams for M 3-15, obtained for three slit positions. As for the case of M 1-32, the emission line shown in these spectra is $[N II]\lambda 6548$. In the central slit position a bright condensation (at a systemic velocity of 96 km s^{-1}) and jets, ending in knots at $\pm 90 \text{ km s}^{-1}$ (relative to the systemic velocity) are seen. In the East and West slit positions we only observe one side of the jet and one knot.

The observations are not calibrated in flux, but we have added a scale in counts. In the observational PV diagrams, the ratio between the brightest and faintest regions is of the order of 30.

¹ IRAF is distributed by the National Optical Astronomy Observatories, which is operated by the Association of Universities for Research in Astronomy, Inc., under contract to the National Science Foundation.

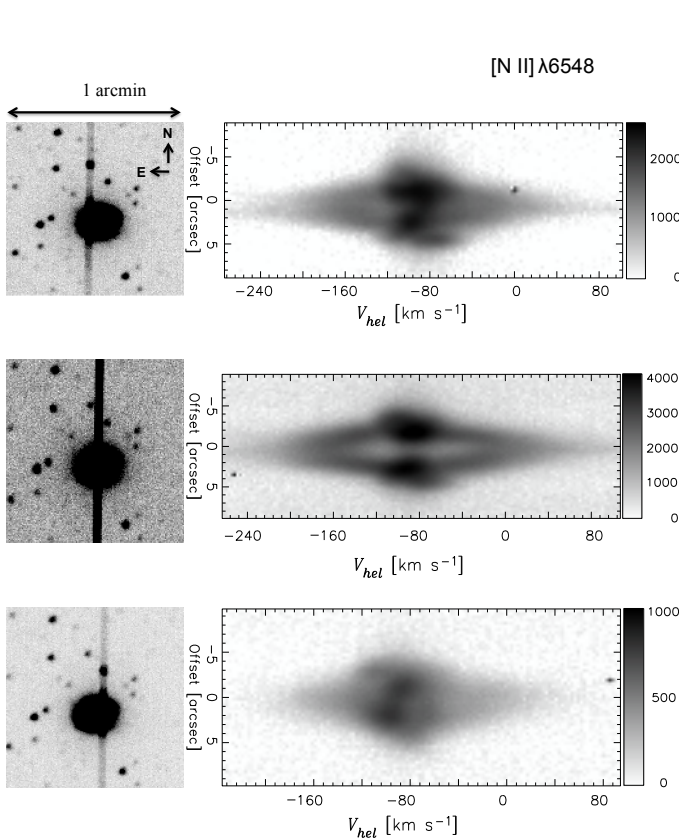


Figure 2. Position-velocity diagrams of M 1-32 in the $[\text{N II}]\lambda 6548$ line, for three positions of the slit (shown in the left frames). The Eastern and Western slits are located at about 2.8 arcsec and 2.5 arcsec (respectively) from the centre of the object. The size of the images is 1.0×1.0 arcmin. In the diagrams to the right, the intense knots correspond to the toroidal component. The wide faint components come from a bipolar jet. The grey scale to the right is the intensity in counts. The ratio between the brightest and faintest regions is of the order of 30.

3 NUMERICAL SIMULATIONS

3.1 The hydrodynamical model and the Yguazú code

We have calculated hydrodynamical models using the code Yguazú. This is a 3D adaptive code which solves the gasdynamic equations using the ‘flux vector splitting’ algorithm of van Leer (1982). Together with these equations, it also integrates a system of equations for atomic/ionic species, which are used for obtaining the cooling function (Raga et al. 2000). For this simulation, we have used the total abundances of C, N, O and S (relative to hydrogen), obtained by García-Rojas et al. (2013).

From the observations it is evident that both objects have a dense torus and that the high velocity wings flow through the poles of the torus. Therefore, in order to calculate a hydrodynamical model for these objects, we have considered a circumstellar medium which was previously swept up by a dense low-velocity wind of an AGB star. Afterwards, a second outflow is launched by the central star. Different

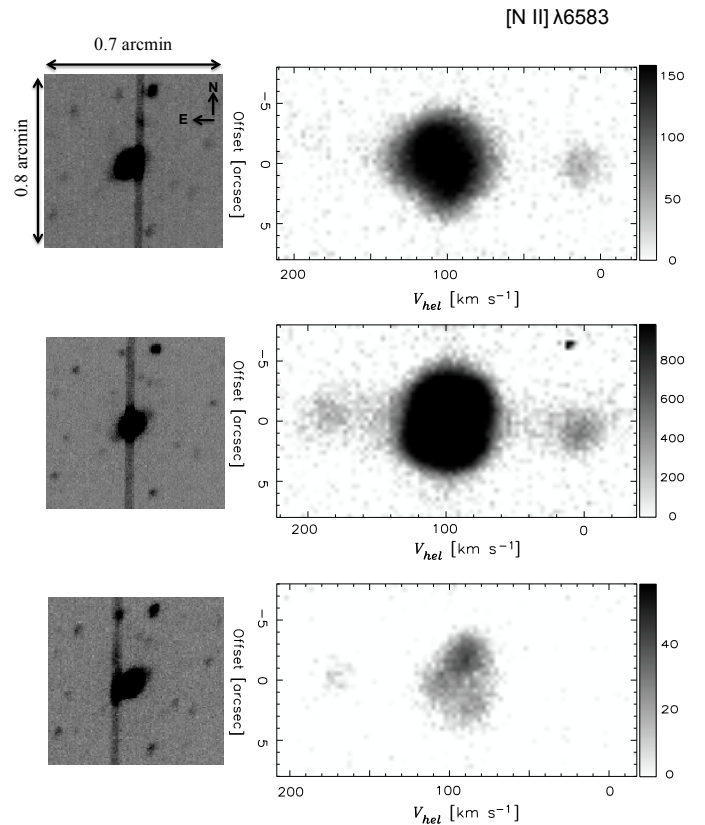


Figure 3. Position-velocity diagrams of M 3-15 in the $[\text{N II}]\lambda 6583$ line, for three slit positions (shown in an image in the left frames). The size of the images is 0.8×0.7 arcmin. The Eastern and Western slits are located at 2.0 arcsec from the centre of the nebula. The intense central emission corresponds to a toroidal component which is more compact than in the case of M 1-32. The wide faint components correspond to a bipolar jet. The grey scale to the right is the intensity in counts. The ratio between the brightest and faintest regions is of the order of 30.

types of second outflow were modeled: an isotropic wind, an anisotropic wind (with anisotropical distributions in density or velocity), a cylindrical jet and a conical jet.

We finally found that the model that best describes the PV diagrams observed for M 1-32 and M 3-15 nebula consists of two components: a dense torus and a bipolar system of conical jets. However, this model does not reproduce the bright regions at radial velocities close to zero, which are observed in the PV diagrams. In order to reconcile observations with models, it was necessary to include the effect of a central star of the nebula, which would ionise the surrounding medium. Due to the fact that the Yguazú hydrodynamical code does not solve the radiative transfer equation, we have included the photoionisation effects of a central source by keeping H, He, C, O, and N at least singly ionised.

3.2 Initial setup

Following Mellema (1995), at the beginning of our simulations, we have imposed on all of the computational domain an AGB wind which has a density distribution given by

$$\rho(r, \theta) = \rho_0 g(\theta) (r_0/r)^2, \quad (1)$$

where $\rho_0 = \dot{M}/(4\pi r_0^2 v)$ is the initial density of the AGB slow wind, with mass loss rate \dot{M} and a terminal velocity v of 20 km s^{-1} . The angular dependence of the wind is given by the parametrized function

$$g(\theta) = 1 - A \left[\frac{1 - \exp(-2B \cos^2 \theta)}{1 - \exp(-2B)} \right], \quad (2)$$

where A determines the ratio between the density at the equator and the pole; and B determines the way the density varies from the equator to the pole, r is the distance from the central star and θ is the polar angle (0° at the pole and 90° at the equator). In the equation 1, r_0 is a reference radius which is equivalent to 5 pixels of the grid at maximum resolution. The values of r_0 employed in our simulations are listed in table 3.

For the case of PN M 1-32 we have chosen $A = 0.9$ and $B = 5$, and for M 3-15 we have chosen $A = 0.99$ and $B = 0.1$. For both models, a temperature of 1000 K was adopted for the AGB wind. In Table 3 we list the values for \dot{M} , the initial jet radius r_j (which was set equal to r_0), the jet velocity v_j , the semi-aperture of the conical jet α , and the size of the computational domain employed for our PN models.

4 RESULTS AND DISCUSSION

Fig. 4 shows the time evolution of the electron density distribution of the models for M 1-32 and M 3-15. Also, this figure shows the velocity field of the flow. A clear bipolar morphology results from the presence of the conical jets. This outflow expands into a latitude-dependent AGB wind, with high densities at the Equator. In order to compare the observations (Figs. 2 and 3) with the hydrodynamical model, we also obtained PV diagrams from the models.

The simulation for M 1-32 was carried out until an integration time of 4500 yr. Synthetic PV diagrams (for the $[\text{N II}]\lambda 6583$ emission line) were obtained considering several slits located at different distances from the symmetry axis of the object. Due to the fact that the observed PV diagrams of this PN are symmetrical on both sides of the axis, we only display the PV diagrams obtained for slits located to the right of the PN source (the same results are obtained if we move the slit to the left). These PV diagrams are shown in Fig. 5.

The bright central knots come from the torus, which has a total diameter of $20''$ and it is at a velocity of 0 km s^{-1} , while the wings (associated with the jet) show velocities ranging up to $\pm 150 \text{ km s}^{-1}$. In these synthetic PV diagrams, for slits located farther away from the centre, the inner zone of the torus is filling up, due to the fact that the slits approach the edge of the PN. In addition, in PV diagram for Fig. 5 d) only part of the jet is seen, giving the appearance that the wings are moving at slow velocities.

For M 1-32, our synthetic PV diagrams (Fig. 5) are in

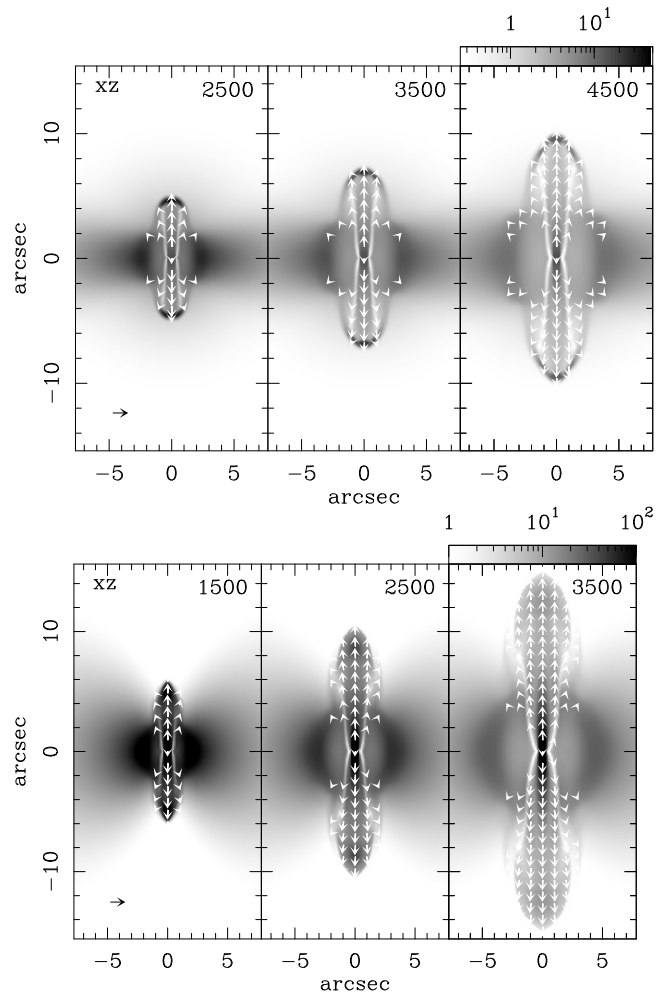


Figure 4. Top: Electron density distribution map (xz -projection), corresponding to the model for M 1-32 at different evolutionary times in yr. Bottom: the same map for M 3-15. The grey scale (given by the bars on the top of the right hand side frames) is given in units of particles cm^{-3} . Both axes are given in units of arcseconds, considering a distance of 4.8 kpc and 6.8 kpc for M 1-32 and M 3-15, respectively. The arrows show the velocity field of the jet. The small arrows at the bottom of the left frames correspond to 200 km s^{-1} .

good agreement with the observational ones (Fig. 2), especially the synthetic PV diagrams labeled a), c) and d) corresponding to slits located on the axis, at $2''$, and at $3''$ from the centre, respectively. We reproduce the central knots corresponding to the dense torus, and the wide wings associated with the jet material.

In our model for M 1-32, the jet axis is nearly pole-on, i.e., at 0° with respect to the line of sight. The synthetic PV diagrams show fast bipolar outflows at velocities of 160 km s^{-1} , with shapes that are similar to the observations (Fig. 2), and a dense torus which expands at velocities of approximately 25 km s^{-1} with respect to the centre of the nebula (also in qualitative agreement with the observations).

The fact that we assume that all of the material in the computational domain is at least singly ionized results in strong emission from the bowshocks at the leading edge of the conical jets. This emission produces the bright knots at

Table 3. Input for hydrodynamical simulations

Name	Computational domain x -, y -, and z -axis, (cm)	A	B	$r_j = r_0$ (cm)	v_j (km s^{-1})	α (degrees)	\dot{M} ($M_\odot \text{ yr}^{-1}$)
M1-32	$(2.25, 2.25, 4.5) \times 10^{18}$	0.9	5	4.4×10^{16}	150	5	5×10^{-6}
M3-15	$(1.57, 1.57, 3.15) \times 10^{18}$	0.99	0.1	3.08×10^{18}	140	5	6×10^{-6}

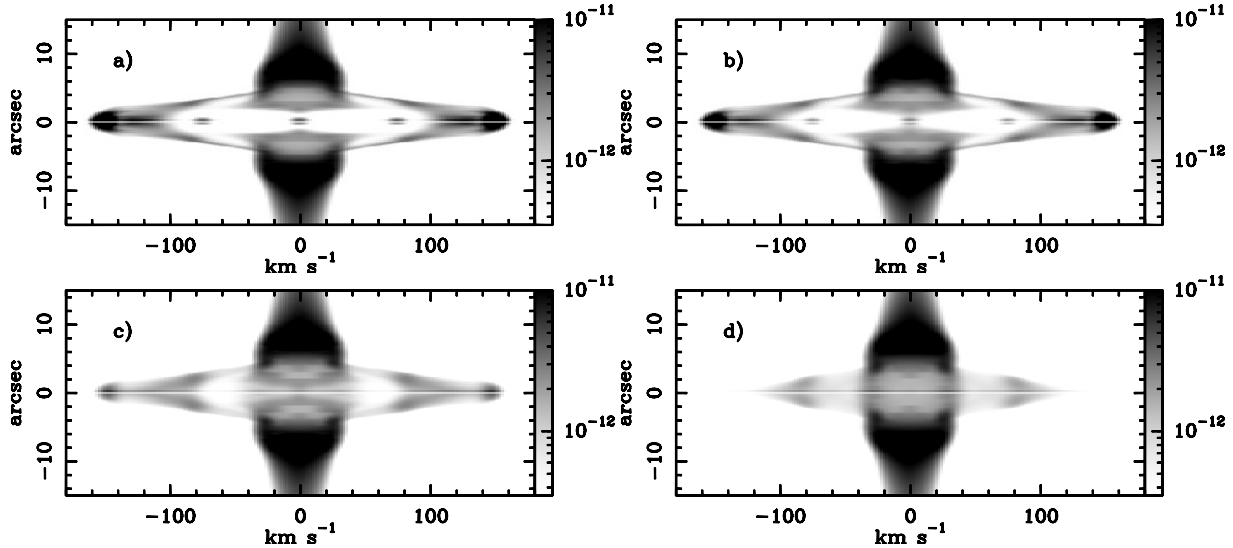


Figure 5. Synthetic position-velocity diagrams of the $[\text{N II}]\lambda 6583$ line, obtained from the hydrodynamical model for M1-32. a) PV diagram for the slit located on the axis of the model. b) Slit at 1 arcsec from the axis. c) Slit located at 2 arcsec from axis. d) Slit at 3 arcsec from the axis. The horizontal and vertical axes represent the velocity in km s^{-1} and the spatial direction in arcsec, respectively. The logarithmic grey scale is given in units of $\text{erg cm}^{-3} \text{ sr}^{-1}$.

radial velocities of $\pm 160 \text{ km s}^{-1}$ in the PV diagrams corresponding to slit position a) and b) (Fig. 5).

M3-15 was modeled with the same hydrodynamical setup as M1-32: a dense torus and a conical jet, but using different parameters. By comparing the images of M1-32 and M3-15 (see Figs. 2 and 3), we note that M3-15 exhibits an elongation in the SE-NW direction. This fact suggests that the jet axis (the z -axis of the computational domain) must be tilted with respect to the North-South direction and to the line of sight. The synthetic PV diagrams displayed in Fig. 6, were obtained after an integration time of 3500 yr, and after applying two rotations to the computational domain. After several tests, we obtained a good agreement with observations if the jet axis was tilted by -55° with respect to the North direction, and at an inclination of 30° with respect to the line of sight. These PV diagrams show a bright condensation corresponding to the torus. The collimated outflows have velocities of the order of 100 km s^{-1} .

Our hydrodynamical model, shown in Fig. 4, has a bipolar structure of conical jets which emerge through the poles of a toroidal structure. Morphologically, M1-32 has been classified as “elliptical” (Stanghellini & Haywood 2010), and M3-15 as L,c (Sahai et al. 2011), meaning that it shows close, collimated lobes, with a “barrel-shaped” central region. In the observations, these objects do not look like bipolar nebulae due to the bipolar lobes are being ejected along or very close to the line of sight. Their bipolarity is only noticed

through the spectroscopic data. Therefore, we propose to call them “spectroscopic bipolars”.

Using the available spectra in The SPM Kinematic Catalogue of Galactic Planetary Nebulae (López et al. 2012), we have found some PNe with similar spectral characteristics to M1-32 and M3-15 (spectra showing outflows). From a sample of 29 objects with [WC] central stars, 10 [WC]PNe are “spectroscopic bipolar nebulae”, that represents 34.4% of the sample. The outflows of these [WC]PNe reach more than 70 km s^{-1} . As an example, in Fig. 7 we present the PV diagram for H1-67 which has a [WO2] central star. Its outflows have a velocity of $\pm 100 \text{ km s}^{-1}$ relative to the system.

From a sample of 34 PNe (taken randomly) with WEL central stars (weak emission line stars), 7 objects have outflows. This represents 20.5% of the sample. Only three of these seven objects (H1-42, NGC 6644 and M3-38) would be “spectroscopic bipolar nebulae” with fast bipolar outflows at about 70 km s^{-1} . A PV diagram for H1-42 is shown in Fig. 7. These three PNe and 10 [WC]PNe mentioned above are good candidates for modelling with our “torus+bipolar outflow” dynamical model.

In addition, from a sample of 36 PNe with normal central stars (taken randomly), 4 have outflows. These outflows show velocities smaller than 50 km s^{-1} . From these four, M1-4 could be explained with the hydrodynamical model presented here but with a slower velocity jet (see Fig. 7). According to these raw statistics, an important fraction of

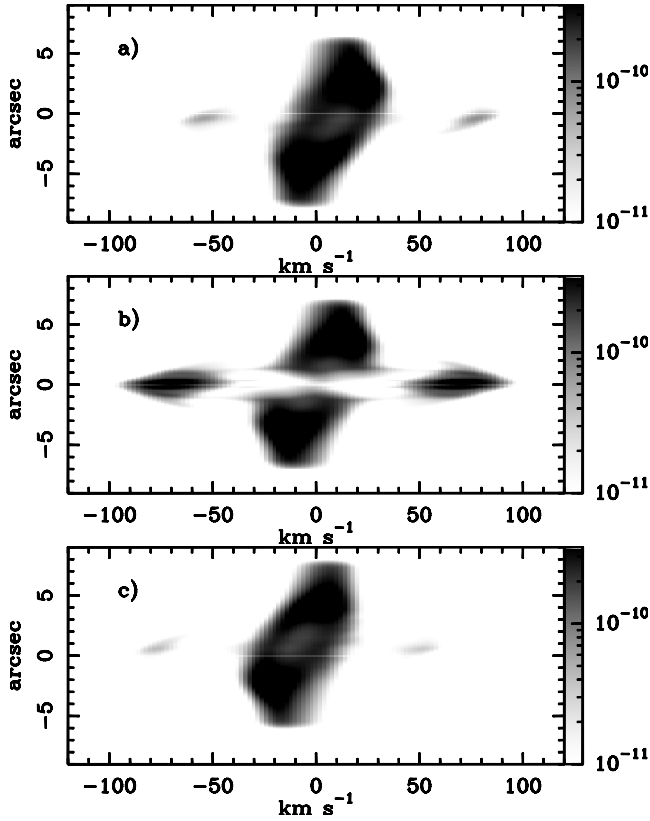


Figure 6. Synthetic [N II] PV diagrams for M3-15. a) PV diagram for slit located at 2.0 arcsec to the right of the source. b) PV diagram for a slit going through the centre of the source. c) PV diagram for a slit at 2.0 arcsec to the left from the source. The horizontal and vertical axes represent the radial velocity in km s^{-1} and the spatial direction in arcsec, respectively. The logarithmic grey scale is given in units of $\text{erg cm}^{-3} \text{sr}^{-1}$.

[WC] type central stars could be producing PNe with high-velocity outflows, which is not the case for PNe around WELS or normal central stars.

5 CONCLUSIONS

With the Yguazú code we have carried out 3D hydrodynamical simulations of a bipolar jet system moving inside an anisotropic AGB wind with a high density at the Equator (producing a dense torus around the central star of a PN). In order to explain the global morphology and the PV diagrams of the PNe M1-32 and M3-15, it was necessary to assume that all of the simulated structure is photoionized by the central star.

The bipolar ejection leaves the central star, expanding through the poles of the torus at high velocities, of the order of 160 km s^{-1} and 100 km s^{-1} for M1-32 and M3-15, respectively. With the simulations we reproduce the observed PV diagrams of these nebulae after an integration time of 4500 yr for M1-32, and 3500 yr for M3-15. These values are in agreement with the age of young PN.

Sahai et al. (2011) classified M3-15 as having close collimated lobes with a close barrel shaped central region, and M1-32 was previously classified as an elliptical. However, spectroscopically we find that both M3-15 and M1-32 show

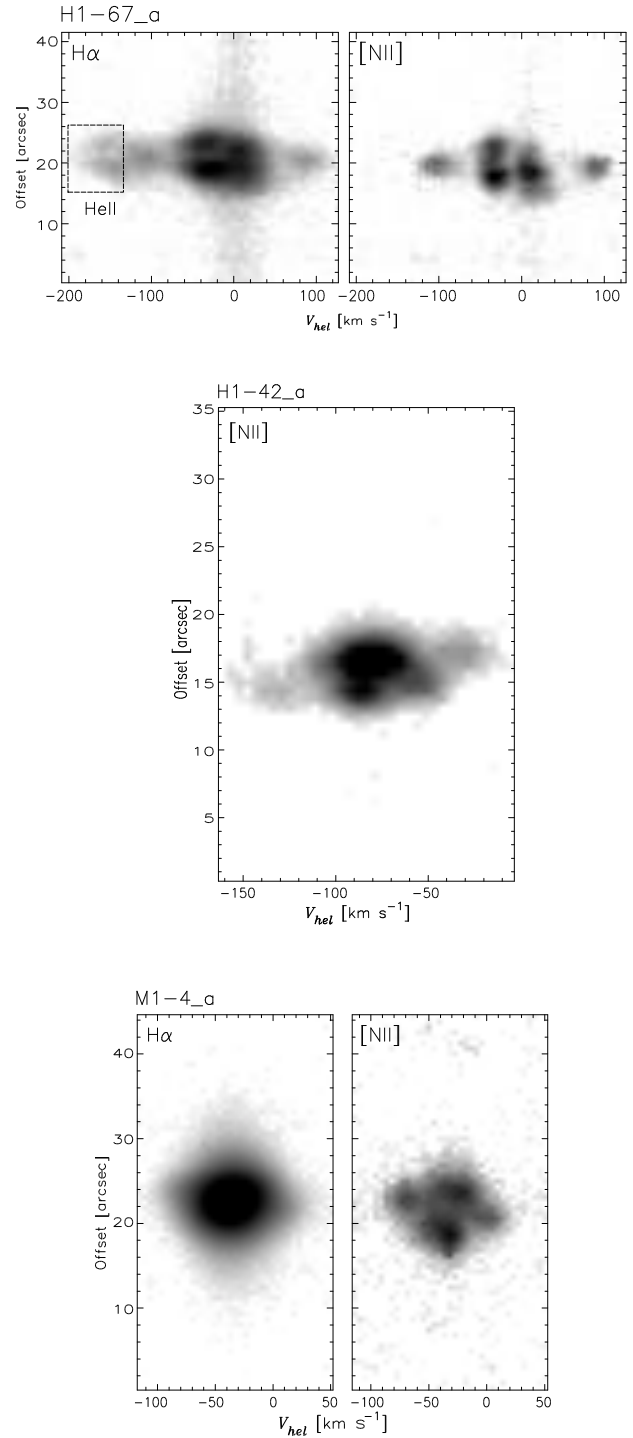


Figure 7. PV diagrams observed for three PNe, obtained from The SPM Kinematic Catalogue of Planetary Nebulae. Top: PN H1-67 with a [WO2] central star, we observe three bright knots at the centre and two faint knots reaching high velocities. Middle: PN H1-42 with a WEL central star, we observe a sphere at the centre and high-velocity outflows. Bottom: PN M1-4 with a normal central star, we observe two bright, inclined knots at the centre, and two faint knots reaching low velocities. These PNe are good candidates for our hydrodynamical model.

a torus and high-velocity bipolar ejections. Therefore, we propose to call them “spectroscopic bipolar nebulae”. As we explained in the introduction bipolar (and multipolar) planetary nebulae can be created by binary stars (see for example, Morris 1987; Soker 1998). Therefore, M1-32 and M3-15 could host a binary system in their centre, which could be confirmed in a future work.

In the kinematical catalogue of Galactic PNe (López et al. 2012) we have found that the spectra of 34.4% of 29 [WC]PNe show outflows at high velocities. Some PNe around WELS or normal central stars also show similar outflows, but with smaller velocities. Therefore, a large fraction of [WC] central stars are producing nebulae with fast, bipolar outflows.

In summary, we have shown that the same physical model, a bipolar jet system moving inside an anisotropic AGB wind (with high density at the Equator, producing a dense torus-like structure) can explain the observed PV diagrams of M1-32 and M3-15 PNe. In future work we intend to model other PNe with similar characteristics.

ACKNOWLEDGMENTS

We would like to thank Fernando Ávila Castro and Dr. Margarita Pereyra for their help in the installation and use on WIP. Helpful comments by Dr. Jorge García-Rojas are deeply acknowledged. We are grateful to Prof. Noam Soker for his comments and suggestions, which allowed to improve the previous version of this manuscript. We acknowledge Enrique Palacios (Cómputo-ICN) for maintaining the Linux servers where the hydrodynamical simulations were carried out. We thank the daytime and night support staff at the OAN-SPM for facilitating and helping to obtain our observations. This work received financial support from DGAPA-PAPIIT grants IN109614, IG100516 and CONACyT grant 167611. J.S.R.-G. acknowledges scholarship from CONACyT-México.

REFERENCES

- Acker A., Neiner C., 2003, AAP, 403, 659
 Akras S., López J. A., 2012, MNRAS, 425, 2197
 Balick B., 1987, AJ, 94, 671
 Balick B., Frank A., 2002, araa, 40, 439
 Bond H. E., 2000, in Kastner J. H., Soker N., Rappaport S., eds, *Asymmetrical Planetary Nebulae II: From Origins to Microstructures* Vol. 199 of *Astronomical Society of the Pacific Conference Series*, . p. 115
 Bond H. E., Liller W., Mannery E. J., 1978, ApJ, 223, 252
 De Marco O., 2009, PASP, 121, 316
 De Marco O., Hillwig T. C., Smith A. J., 2008, AJ, 136, 323
 Dennis T. J., Cunningham A. J., Frank A., Balick B., Blackman E. G., Mitran S., 2008, ApJ, 679, 1327
 Douchin D., De Marco O., Jacoby G. H., Hillwig T. C., Frew D. J., Bojičić I., Jasniewicz G., Parker Q. A., 2013, *Central European Astrophysical Bulletin*, 37, 391
 García-Arredondo F., Frank A., 2004, ApJ, 600, 992
 García-Rojas J., Peña M., Morisset C., Delgado-Inglada G., Mesa-Delgado A., Ruiz M. T., 2013, AAP, 558, A122
 García-Segura G., Langer N., Różyczka M., Franco J., 1999, ApJ, 517, 767
 García-Segura G., Villaver E., Langer N., Yoon S.-C., Manchado A., 2014, ApJ, 783, 74
 Karakas A. I., 2010, MNRAS, 403, 1413
 Koesterke L., 2001, APSS, 275, 41
 Livio M., Salzman J., Shaviv G., 1979, MNRAS, 188, 1
 López J. A., Richer M. G., García-Díaz M. T., Clark D. M., Meaburn J., Riesgo H., Steffen W., Lloyd M., 2012, RMxAA, 48, 3
 Manchado A., Guerrero M. A., Stanghellini L., Serrà Ricart M., 1996, *The IAC morphological catalog of northern Galactic planetary nebulae*
 Meaburn J., López J. A., Gutiérrez L., Quiróz F., Murillo J. M., Valdéz J., Pedrayez M., 2003, RMxAA, 39, 185
 Medina S., Peña M., Morisset C., Stasińska G., 2006, RMxAA, 42, 53
 Mellema G., 1995, MNRAS, 277, 173
 Miszalski B., Acker A., Moffat A. F. J., Parker Q. A., Udalski A., 2009, AAP, 496, 813
 Morgan J. A., 1995, in Shaw R. A., Payne H. E., Hayes J. J. E., eds, *Astronomical Data Analysis Software and Systems IV* Vol. 77 of *Astronomical Society of the Pacific Conference Series*, . p. 129
 Morris M., 1987, PASP, 99, 1115
 Nordhaus J., Blackman E. G., Frank A., 2007, MNRAS, 376, 599
 Parker Q. A., Acker A., Frew D. J., Hartley M., Peyaud A. E. J., Ochsenbein F., Phillipps S., Russeil D., Beaulieu S. F., Cohen M., Köppen J., Miszalski B., Morgan D. H., Morris R. A. H., Pierce M. J., Vaughan A. E., 2006, MNRAS, 373, 79
 Pascoli G., 1992, PASP, 104, 350
 Peña M., Rechy-García J. S., García-Rojas J., 2013, RMxAA, 49, 87
 Peimbert M., 1990, *Reports on Progress in Physics*, 53, 1559
 Raga A. C., Navarro-González R., Villagrán-Muniz M., 2000, RMxAA, 36, 67
 Riera A., Velázquez P. F., Raga A. C., Estalella R., Castañón A., 2014, AAP, 561, A145
 Sahai R., Morris M. R., Villar G. G., 2011, AJ, 141, 134
 Sahai R., Trauger J. T., 1998, AJ, 116, 1357
 Soker N., 1998, ApJ, 496, 833
 Soker N., 2006, PASP, 118, 260
 Soker N., Harpaz A., 1992, PASP, 104, 923
 Soker N., Livio M., 1994, ApJ, 421, 219
 Soker N., Rappaport S., 2000, ApJ, 538, 241
 Stanghellini L., Haywood M., 2010, ApJ, 714, 1096
 Tocknell J., De Marco O., Wardle M., 2014, MNRAS, 439, 2014
 van Leer B., 1982, in Krause E., ed., *Numerical Methods in Fluid Dynamics* Vol. 170 of *Lecture Notes in Physics*, Berlin Springer Verlag, . pp 507–512
 Velázquez P. F., Riera A., Raga A. C., Toledo-Roy J. C., 2014, ApJ, 794, 128
 Weidmann W. A., Gamen R., 2011, AAP, 531, A172